View metadata, citation and similar papers at core.ac.uk

brought to you by CORE

provided by Haverford College: Haverford Scholarship

Haverford College

Haverford Scholarship

Faculty Publications

Astronomy

2012

The Atacama Cosmology Telescope: High-Resolution Sunyaev-Zel'dovich Array Observations of Act Sze-Selected Clusters from the Equatorial Strip

Erik D. Reese

Tony Mrosckowski

Felipe Menanteau

Bruce Partridge
Haverford College, bpartrid@haverford.edu

Follow this and additional works at: https://scholarship.haverford.edu/astronomy_facpubs

Repository Citation

The Atacama Cosmology Telescope: High-resolution Sunyaev-Zel'dovich Array Observations of ACT SZE-selected Clusters from the Equatorial Strip Reese, Erik D.; Mroczkowski, Tony; Menanteau, Felipe; Hilton, Matt; Sievers, Jonathan; Aguirre, Paula; Appel, John William; Baker, Andrew J.; Bond, J. Richard; Das, Sudeep; Devlin, Mark J.; Dicker, Simon R.; Dünner, Rolando; Essinger-Hileman, Thomas; Fowler, Joseph W.; Hajian, Amir; Halpern, Mark; Hasselfield, Matthew; Hill, J. Colin; Hincks, Adam D.; Huffenberger, Kevin M.; Hughes, John P.; Irwin, Kent D.; Klein, Jeff; Kosowsky, Arthur; Lin, Yen-Ting; Marriage, Tobias A.; Marsden, Danica; Moodley, Kavilan; Niemack, Michael D.; Nolta, Michael R.; Page, Lyman A.; Parker, Lucas; Partridge, Bruce; Rojas, Felipe; Sehgal, Neelima; Sifón, Cristóbal; Spergel, David N.; Staggs, Suzanne T.; Swetz, Daniel S.; Switzer, Eric R.; Thornton, Robert; Trac, Hy; Wollack, Edward J. The Astrophysical Journal, Volume 751, Issue 1, article id. 12, 12 pp. (2012).

This Journal Article is brought to you for free and open access by the Astronomy at Haverford Scholarship. It has been accepted for inclusion in Faculty Publications by an authorized administrator of Haverford Scholarship. For more information, please contact nmedeiro@haverford.edu.

Haverford College
Haverford Scholarship

Faculty Publications | Astronomy

2012

The Atacama Cosmology Telescope: High-Resolution Sunyaev-Zel'dovich Array Observations of Act Sze-Selected Clusters from the Equatorial Strip

Erik D. Reese

Tony Mrosckowski

Felipe Menanteau

R. Bruce Partridge
Haverford College

Follow this and additional works at: http://scholarship.haverford.edu/astronomy_facpubs

Repository Citation

The Atacama Cosmology Telescope: High-resolution Sunyaev-Zel'dovich Array Observations of ACT SZE-selected Clusters from the Equatorial Strip Reese, Erik D.; Mroczkowski, Tony; Menanteau, Felipe; Hilton, Matt; Sievers, Jonathan; Aguirre, Paula; Appel, John William; Baker, Andrew J.; Bond, J. Richard; Das, Sudeep; Devlin, Mark J.; Dicker, Simon R.; Dünner, Rolando; Essinger-Hileman, Thomas; Fowler, Joseph W.; Hajian, Amir; Halpern, Mark; Hasselfield, Matthew; Hill, J. Colin; Hincks, Adam D.; Huffenberger, Kevin M.; Hughes, John P.; Irwin, Kent D.; Klein, Jeff; Kosowsky, Arthur; Lin, Yen-Ting; Marriage, Tobias A.; Marsden, Danica; Moodley, Kavilan; Niemack, Michael D.; Nolta, Michael R.; Page, Lyman A.; Parker, Lucas; Partridge, Bruce; Rojas, Felipe; Sehgal, Neelima; Sifón, Cristóbal; Spergel, David N.; Staggs, Suzanne T.; Swetz, Daniel S.; Switzer, Eric R.; Thornton, Robert; Trac, Hy; Wollack, Edward J. The Astrophysical Journal, Volume 751, Issue 1, article id. 12, 12 pp. (2012).

This Journal Article is brought to you for free and open access by the Astronomy at Haverford Scholarship. It has been accepted for inclusion in Faculty Publications by an authorized administrator of Haverford Scholarship. For more information, please contact nmedeiro@haverford.edu.

The Astrophysical Journal, 751:12 (12pp), 2012 May 20 doi:10.1088/0004-637X/751/1/12
© 2012. The American Astronomical Society. All rights reserved. Printed in the U.S.A.

THE ATACAMA COSMOLOGY TELESCOPE: HIGH-RESOLUTION SUNYAEV–ZEL'DOVICH ARRAY OBSERVATIONS OF ACT SZE-SELECTED CLUSTERS FROM THE EQUATORIAL STRIP

Erik D. Reese[1], Tony Mroczkowski [1,23], Felipe Menanteau[2], Matt Hilton[3], Jonathan Sievers[4], Paula Aguirre[5], John William Appel[6], Andrew J. Baker[2], J. Richard Bond[4], Sudeep Das[6,7,8], Mark J. Devlin[1], Simon R. Dicker[1], Rolando Dünner[5], Thomas Essinger-Hileman[6], Joseph W. Fowler[8,9], Amir Hajian[4,6,8], Mark Halpern[10], Matthew Hasselfield[10], J. Colin Hill[8], Adam D. Hincks[6], Kevin M. Huffenberger[11], John P. Hughes[2], Kent D. Irwin[9], Jeff Klein[1], Arthur Kosowsky[12], Yen-Ting Lin[13,14], Tobias A. Marriage[8,15], Danica Marsden[1], Kavilan Moodley[16], Michael D. Niemack[6,9], Michael R. Nolta[4], Lyman A. Page[6], Lucas Parker[6], Bruce Partridge[17], Felipe Rojas[5], Neelima Sehgal[18], Cristóbal Sifón[5], David N. Spergel[8], Suzanne T. Staggs[6], Daniel S. Swetz[1,9], Eric R. Switzer[1,19], Robert Thornton[1,20], Hy Trac[21], and Edward J. Wollack[22]

[1] Department of Physics and Astronomy, University of Pennsylvania, 209 South 33rd Street, Philadelphia, PA 19104, USA
[2] Department of Physics and Astronomy, Rutgers, The State University of New Jersey, Piscataway, NJ 08854-8019, USA
[3] School of Physics and Astronomy, University of Nottingham, University Park, Nottingham, NG7 2RD, UK
[4] Canadian Institute for Theoretical Astrophysics, University of Toronto, Toronto, ON M5S 3H8, Canada
[5] Departamento de Astronomía y Astrofísica, Facultad de Física, Pontificia Universidad Católica de Chile, Casilla 306, Santiago 22, Chile
[6] Joseph Henry Laboratories of Physics, Jadwin Hall, Princeton University, Princeton, NJ 08544, USA
[7] Berkeley Center for Cosmological Physics, LBL and Department of Physics, University of California, Berkeley, CA 94720, USA
[8] Department of Astrophysical Sciences, Peyton Hall, Princeton University, Princeton, NJ 08544, USA
[9] NIST Quantum Devices Group, 325 Broadway Mailcode 817.03, Boulder, CO, 80305, USA
[10] Department of Physics and Astronomy, University of British Columbia, Vancouver, BC V6T 1Z4, Canada
[11] Department of Physics, University of Miami, Coral Gables, FL 33124, USA
[12] Department of Physics and Astronomy, University of Pittsburgh, Pittsburgh, PA 15260, USA
[13] Institute for the Physics and Mathematics of the Universe, The University of Tokyo, Kashiwa, Chiba 277-8568, Japan
[14] Institute of Astronomy and Astrophysics, Academia Sinica, Taipei, Taiwan
[15] Department of Physics and Astronomy, The Johns Hopkins University, 3400 North Charles Street, Baltimore, MD 21218-2686, USA
[16] Astrophysics and Cosmology Research Unit, School of Mathematical Sciences, University of KwaZulu-Natal, Durban 4041, South Africa
[17] Department of Physics and Astronomy, Haverford College, Haverford, PA 19041, USA
[18] Kavli Institute for Particle Astrophysics and Cosmology, Stanford University, Stanford, CA 94305-4085, USA
[19] Kavli Institute for Cosmological Physics, Laboratory for Astrophysics and Space Research, 5620 South Ellis Avenue, Chicago, IL 60637, USA
[20] Department of Physics, West Chester University of Pennsylvania, West Chester, PA 19383, USA
[21] Department of Physics, Carnegie Mellon University, Pittsburgh, PA 15213, USA
[22] NASA/Goddard Space Flight Center, Code 553/665, Greenbelt, MD 20771, USA
Received 2011 August 11; accepted 2012 March 30; published 2012 April 30

ABSTRACT

We present follow-up observations with the Sunyaev–Zel'dovich Array (SZA) of optically confirmed galaxy clusters found in the equatorial survey region of the Atacama Cosmology Telescope (ACT): ACT-CL J0022–0036, ACT-CL J2051+0057, and ACT-CL J2337+0016. ACT-CL J0022–0036 is a newly discovered, massive ($\simeq 10^{15}\ M_{\odot}$), high-redshift ($z = 0.81$) cluster revealed by ACT through the Sunyaev–Zel'dovich effect (SZE). Deep, targeted observations with the SZA allow us to probe a broader range of cluster spatial scales, better disentangle cluster decrements from radio point-source emission, and derive more robust integrated SZE flux and mass estimates than we can with ACT data alone. For the two clusters we detect with the SZA we compute integrated SZE signal and derive masses from the SZA data only. ACT-CL J2337+0016, also known as A2631, has archival *Chandra* data that allow an additional X-ray-based mass estimate. Optical richness is also used to estimate cluster masses and shows good agreement with the SZE and X-ray-based estimates. Based on the point sources detected by the SZA in these three cluster fields and an extrapolation to ACT's frequency, we estimate that point sources could be contaminating the SZE decrement at the $\lesssim$20% level for some fraction of clusters.

Key words: cosmic background radiation – cosmology: observations – galaxies: clusters: general – techniques: interferometric – X-rays: galaxies: clusters

Online-only material: color figures

1. INTRODUCTION

The Sunyaev–Zel'dovich effect (SZE) is a small (typically $\lesssim$1 mK) distortion of the cosmic microwave background (CMB) spectrum caused by the inverse Compton scattering of CMB photons off energetic electrons of the hot intracluster medium of galaxy clusters (Zeldovich & Sunyaev 1969; Sunyaev & Zel'dovich 1970, 1972; for reviews see, Sunyaev & Zeldovich 1980; Rephaeli 1995; Birkinshaw 1999; Carlstrom et al. 2002). The redshift independence of the SZE makes it a potentially powerful tool with which to search for galaxy clusters, especially in the distant universe. Abundances of clusters probe the growth of structure and have placed useful constraints on the fluctuation amplitude, σ_8, and the matter density, Ω_M (e.g., Henry & Arnaud 1991; Viana & Liddle 1996; Bahcall et al. 1997; Eke et al. 1998; Borgani et al. 2001; Reiprich & Böhringer 2002; Schuecker et al. 2003; Henry 2004; Mantz et al. 2008, 2010; Vikhlinin et al. 2009; Rozo et al. 2010; Vanderlinde et al. 2010; Sehgal

[23] Einstein Postdoctoral Fellow.

et al. 2011). The evolution of cluster abundance with redshift is one of the few probes of the growth of structure and has the potential to tightly constrain cosmological parameters and provide insight into the equation of state of the dark energy (e.g., Bartlett & Silk 1994; Holder et al. 2000; Haiman et al. 2001; Majumdar & Mohr 2004). The biggest challenge to realizing the cosmological potential of cluster surveys is relating cluster mass to an observable such as integrated SZE signal. Well-determined masses for even a subsample of clusters can significantly improve parameter constraints (e.g., Majumdar & Mohr 2004).

The last few years have seen significant advances in surveys using the SZE. The Atacama Cosmology Telescope (ACT; Fowler et al. 2007), the South Pole Telescope (Carlstrom et al. 2011), and the *Planck* satellite (Planck Collaboration et al. 2011a) are, for the first time, producing catalogs of galaxy clusters discovered through the SZE (Vanderlinde et al. 2010; Marriage et al. 2011a; Planck Collaboration et al. 2011b; Williamson et al. 2011). The fast mapping speeds and improved sensitivities of these instruments have enabled them to survey large regions of the sky with sufficient depth to detect massive clusters, but their limited angular resolutions ($\gtrsim 1'$) do not allow detailed studies of cluster astrophysics with their data alone.

We have performed initial follow-up observations with the Sunyaev–Zel'dovich Array (SZA) of three optically confirmed ACT clusters in ACT's equatorial strip. The value of SZE follow-up of SZE-selected clusters has recently been demonstrated for clusters selected by *Planck* (see Planck Collaboration et al. 2011b; AMI Consortium et al. 2011; Story et al. 2011; Sayers et al. 2012; Muchovej et al. 2012). Deep, targeted SZA observations of ACT clusters provide higher sensitivity over a broader range of cluster spatial scales than that of ACT. In addition, the spatial filtering of the interferometer provides a method of cleanly disentangling radio point-source emission from the cluster SZE signal. ACT observational details and target selection are presented in Section 2. SZA and *Chandra* observations and data reduction are described in Sections 3.1 and 3.3, respectively. The analysis method and results are reported in Section 4, the implications in Section 5, and conclusions in Section 6.

Throughout this paper, all uncertainties are reported at 68% confidence and we adopt a flat, Λ-dominated cosmology with $\Omega_M = 0.3$, $\Omega_\Lambda = 0.7$, and $H_0 = 70$ km s^{-1} Mpc^{-1} consistent with recent *Wilkinson Microwave Anisotropy Probe* (*WMAP*) results (Komatsu et al. 2011, 2009).

2. ACT TARGET SELECTION

The ACT is a 6 m diameter telescope located at an elevation of 5200 m in the Atacama desert of Chile. Three 1024-element transition-edge-sensing bolometer arrays operate at 148, 218, and 277 GHz and survey large regions of the sky mainly in two regions, a southern strip centered at declination $-52.^\circ5$ and in an equatorial strip that encompasses the Sloan Digital Sky Survey (SDSS) Stripe 82 (hereafter S82; Abazajian et al. 2009; Annis et al. 2012). For the ACT instrument, observation, reduction, and calibration details see Fowler et al. (2007), Swetz et al. (2011), Das et al. (2011), and Hajian et al. (2011). Initial results from the ACT southern strip include CMB power spectra (Fowler et al. 2010; Das et al. 2011), compact source (Marriage et al. 2011b) and cluster catalogs (Marriage et al. 2011a), cluster follow-up (Menanteau et al. 2010a), and analysis of the cosmological implications of CMB power spectra (Dunkley et al. 2011) and cluster yields (Sehgal et al. 2011).

A matched filter method (Haehnelt & Tegmark 1996; Herranz et al. 2002; Melin et al. 2006) is used for cluster detection to produce a cluster catalog (for ACT-specific details, see Marriage et al. 2011a). We focus on the S82 region as optical data are available from which we measure cluster redshifts and estimate cluster masses via richness and luminosity. High S/N clusters are the most massive systems, which provide the most leverage on cosmological constraints and will form ACT's core sample that will be used to derive cosmological parameters from cluster counts. We chose three preliminary high signal-to-noise (S/N $\gtrsim$ 5) cluster detections from the S82 region for follow-up as a pilot study for SZA observations; these were ACT-CL J0022–0036, ACT-CL J2051+0057, and ACT-CL J2337+0016. We will refer to these clusters as ACTJ0022, ACTJ2051, and A2631, where ACT-CL J2337+0016 is a previously known Abell cluster. The upper row of panels of Figure 1 shows the SZE images of these three fields expressed as Compton-y (see Equation (2)) made from recent ACT maps. ACTJ0022 is a new high-redshift cluster found by ACT through the SZE. ACTJ0022 was spectroscopically confirmed at $z = 0.81$ from long slit observations of the brightest cluster galaxy (BCG) conducted at the Apache Point and Gemini South Observatories (more details on these observations will be described in F. Menanteau et al. 2012, in preparation, where we present the X-ray and optical properties of the S82 ACT clusters). The S82 data provide the spectroscopic redshift, 0.33, for ACTJ2051 and A2631 has a spectroscopic redshift of 0.27 (Struble & Rood 1999). New maps produced with the full ACT equatorial data set reveal ACTJ2051 to be lower significance (S/N $\simeq$ 4) than inferred from the preliminary maps. Table 1 lists the clusters, alternate names, and redshifts.

3. DATA

3.1. SZA Observations

The SZA is an eight-element interferometer with 3.5 m diameter dishes operating at 30 and 90 GHz. It has an 8 GHz bandwidth (sixteen 500 MHz channels) and is located at an altitude of 2200 m in the Inyo Mountains of California. Our observations use the 30 GHz system, which has a $10.'5$ FWHM primary beam (field of view). Typical system temperatures are $T_{\rm sys} \simeq$ 40–50 K, including atmospheric contributions. Six of the antennas are placed in a compact configuration to maximize cluster sensitivity, while two are deployed at longer baselines to provide higher resolution data. The spatial filtering of the interferometer allows one to disentangle the small-scale, positive point-source emission from the large-scale, negative SZE signal at these frequencies (for an example in a similar context see Reese et al. 2002). The SZA has become part of the Combined Array for Research in Millimeter-wave Astronomy (CARMA) and our data were taken both before and after the CARMA transition.

The SZA observed the three ACT clusters between March and May and between 2010 August and September. A bright quasar was observed every 30 minutes, for about 3 minutes integration time, to monitor the system gain and phase during each observation. Since the fluxes of quasars can be variable on timescales of days or months, these sources only serve as secondary calibrators. We discuss absolute calibration in Section 3.2.

Pre-CARMA data are reduced using a suite of MATLAB routines developed by the SZA collaboration (e.g., Muchovej et al. 2007). Post-CARMA data are reduced using Miriad (Sault et al.

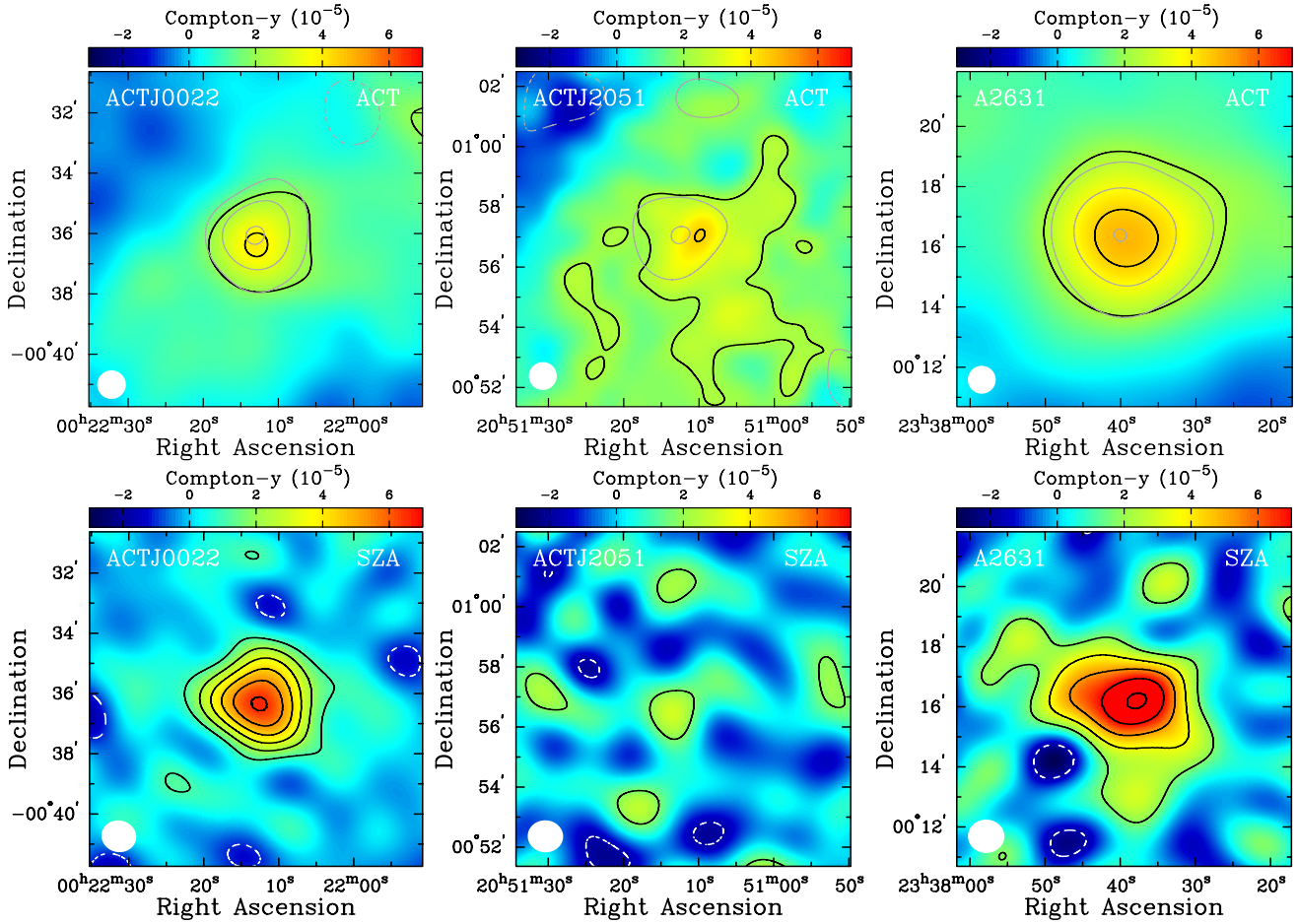

Figure 1. Upper: ACT Compton-y images of the three optically confirmed clusters made from recent ACT maps. We fit (excluding the cluster region in the fit) and remove a quadratic polynomial from the data, smooth with a Gaussian, and resample to smaller pixels. The contours are multiples of twice the rms of each map (black). Also shown are contours from the match filtered map (gray) as multiples of twice the rms. Lower: deconvolved SZA images of the three cluster fields in units of Compton-y. The SZA images are made with short baseline data <2 kλ after removal of point sources. Contours are multiples of twice the rms of each map (for details of the SZA observations presented here, see Table 1). The color scales are in units of 10^{-5} Compton-y, and solid (dashed) lines represent positive (negative) signal. All figures cover the same angular scale (11′ on a side) and are on the same color scale to facilitate comparison. The FWHM of the effective resolution (synthesized beam for the SZA) is shown in the lower left corner of each panel. For visualization purposes the SZA images incorporate only the low-resolution SZA data and the effective beams reflect this choice. The SZA data analysis (Section 4) uses the data in its entirety. ACTJ0022 and A2631 both yield high S/N detections. ACTJ2051 is not detected by the SZA, which is consistent with its lower SZE signal in the current ACT maps (shown here) and with that expected from optical data (see Section 5). In general, the qualitative agreement between the ACT and SZA data is good.

(A color version of this figure is available in the online journal.)

Table 1
SZE Image Statistics

Cluster	Other Name	z	Timing[a]	$t_{\rm int}$[b]	Low Resolution (r_{uv} < 2 kλ)			High Resolution (r_{uv} > 2 kλ)	
					σ	Beam	$\sigma_{\rm CMB}$	σ	Beam
				(hr)	(μJy beam^{-1})	($''\times''$)	(μK)	(μJy beam^{-1})	($''\times''$)
ACT-CL J0022–0036		0.81	pre	15.7	240	94 × 107	38	230	17 × 20
ACT-CL J0022–0036			post	21.8	220	91 × 101	38	230	16 × 20
ACT-CL J2051+0057		0.33	pre	6.7	350	89 × 118	52	300	15 × 22
ACT-CL J2051+0057			post	26.9	230	90 × 105	38	230	16 × 20
ACT-CL J2337+0016	A2631	0.27	post	26.6	240	97 × 106	37	210	17 × 19

Notes.
[a] Pre- and post-CARMA transition of the integration of SZA with CARMA.
[b] Effective on-source integration time accounting for excised data.

1995). Data are excised when one telescope shadows another, when cluster field data are not straddled by two phase calibrator observations, when there are anomalous changes in instrumental response between calibrator observations, when the system temperature changes dramatically between integrations, or when there is spurious correlation.

The Fourier plane is also known as the u–v plane, where (u, v) are the Fourier conjugate variables to right ascension and declination, respectively. We define the radius in the u–v plane as $r_{uv} = \sqrt{u^2 + v^2}$, which corresponds to the baseline length in units of the observation wavelength, λ. The configurations used for these observations produce a break in u–v coverage

at 2 kλ, with similar sensitivities for the low ($r_{uv} < 2$ kλ) and high ($r_{uv} > 2$ kλ) resolution data (15 short and 13 long baselines). Table 1 summarizes the on-source integration times, and (for the high and low-resolution data separately) sensitivities and the FWHMs of the synthesized beams (effective resolution). The rms map noise, $\sigma_{\rm CMB}$, in CMB temperature units for the given synthesized beams, is also given for the low-resolution maps. The total integration times reported correspond to the equivalent time that the full eight-element, 8 GHz bandwidth SZA spent on each cluster (accounting for excised data).

Data visualization is done with Difmap (Shepherd 1997). Identification of point sources in the field is performed with the high-resolution ($r_{uv} > 2$ kλ) data. Point sources are modeled to remove them from the data, and the low-resolution data ($r_{uv} < 2$ kλ) are then deconvolved to produce images of the cluster fields with sources subtracted. We present deconvolved images of the point-source-removed SZA observations as a measure of the data quality. The model fitting is performed in the Fourier plane directly. The cluster and any point sources in the field are modeled simultaneously using the data in its entirety. Modeling of the cluster and point sources is discussed in Section 4.1 and results are discussed in Section 4.2.

The lower panels in Figure 1 show the deconvolved SZA images of the three cluster fields after removal of the point sources. Contours are multiples of twice the rms noise in each map, and the color scale is in units of Compton-y. The FWHM of the synthesized beam (effective resolution) is shown in the lower left of each panel. The images all cover the same angular scale (11′ on a side) and have the same color scale to facilitate comparison. The ACTJ0022 and A2631 fields reveal high-significance SZA detections. The point sources in the ACTJ2051 field are used both to strengthen our calibration of the SZA data and to better assess SZE decrement contamination due to such sources.

3.2. SZA Calibration

Pre-CARMA SZA operations routinely monitored Mars for absolute calibration (e.g., Muchovej et al. 2007). In the period right after the SZA-CARMA merger, standard calibration protocols had not yet been implemented. Therefore, though the system gains are stable, the absolute calibration is off by an arbitrary multiplicative factor. We calibrate the transitional post-CARMA data using radio sources observed both before and after the integration to derive an average calibration factor that is applied to the data. This is non-ideal because the sources can vary; however, we note that on average we do not expect the source flux densities to exhibit any particular trend upward or downward over time, so the average ratio of several sources pre- and post-CARMA may be expected to follow any changes in calibration. The cluster signal will remain constant, so we can validate our calibration by fitting the same model to the pre- and post-CARMA data and comparing the central Compton-y values.

The ACTJ0022 and ACTJ2051 fields have both pre- and post-CARMA data. Two point sources are detected in each field. For the calibration analysis, point-source models are fit to the data. A cluster model is simultaneously fit to the ACTJ0022 data. A Markov Chain Monte Carlo (MCMC) analysis is performed to derive flux densities and uncertainties (model and fitting details are described in Section 4.1). Ratios of pre- to post-CARMA flux densities are computed. The flux densities and ratios are summarized in Table 2. The average ratio is 1.5 ± 0.1, computed with an inverse variance weighting. There is a wide source-to-source variation in the ratios, which range between 1.2 and 2.0, though the uncertainties on the ratios are relatively large and the largest discrepancy is $<2\sigma$. Our average ratio is consistent with the rescaling (≈1.4) found by members of the CARMA collaboration (T. Plagge 2011, private communication).

Table 2
Pre- and Post-CARMA Point-source Flux Densities

Field	$F_\nu^{\rm pre}$ (mJy)	$F_\nu^{\rm post}$ (mJy)	Ratio
ACTJ0022	0.95 ± 0.20	0.80 ± 0.14	1.19 ± 0.30
	1.07 ± 0.18	0.65 ± 0.13	1.65 ± 0.36
ACTJ2051	8.88 ± 0.33	5.03 ± 0.17	1.77 ± 0.32
	3.66 ± 1.36	2.49 ± 0.61	1.47 ± 1.05
Weighted average			1.51 ± 0.07

The cluster SZE signal will not change, but comparisons are complicated by its extended structure. We also fit the same β-model (fixed core radius and power-law index) to the pre- and post-CARMA data for ACTJ0022. The ratio of the central Compton-y parameters also yields the same factor of 1.5. That the cluster normalizations yield the same calibration scaling as the point sources lend some support to our simple approach. As a result, the post-CARMA data are simply scaled by 1.5 and used for the analysis. Note that the rms values in Table 1 correspond to the scaled post-CARMA data. The pre-CARMA data absolute flux calibration is known to better than 10% (Muchovej et al. 2007). Given the large scatter in the flux density ratios, we adopt a conservative 20% calibration uncertainty to account for potential calibration systematics.

3.3. Chandra Observations of A2631

ACTJ2337 is the Abell cluster A2631, which has publicly available *Chandra* X-ray observations. The data consist of two ACIS-I observations, ObsIDs 3248 and 11728, of durations 9 and 17 ks, respectively. The data are reduced starting with the level 1 events file using CIAO 4.3 and calibration database version 4.4.1. Standard corrections are applied, along with light curve filtering and other standard processing (for reduction details see Reese et al. 2010). The *Chandra* images of A2631 are made by binning the 0.7–7.0 keV data to 1.″968 pixels and exposure maps are computed at 1 keV. The images and exposure maps from the two observations are combined, and a wavelet-based source detector is used on the combined image and exposure map to identify and generate a list of potential point sources. The list is used as the basis of our point-source mask.

Figure 2 shows the smoothed *Chandra* data (color) along with the deconvolved SZA data (contours). The color scale shows *Chandra* counts and the contours are multiples of twice the rms of the SZA map. The FWHM of the synthesized beam (effective resolution) is shown in the lower left corner. The same E–W elongation seen in the SZA data is seen in the *Chandra* data as well, and the peaks in the SZE and X-ray images align.

4. ANALYSIS

4.1. Method

We fit cluster models to the data and derive parameters from the best-fit models. ACTJ0022 has no X-ray data and we fit models to the SZE data only. A2631 has both SZA and *Chandra* data and we perform three complementary analyses using

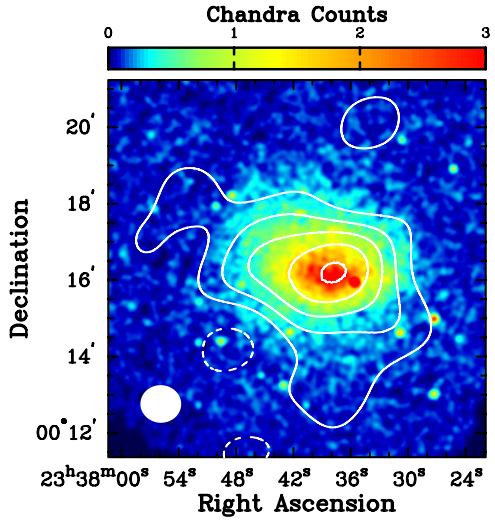

Figure 2. Deconvolved SZA image of A2631 (contours) on the smoothed *Chandra* counts image (color). Contours are multiples of twice the rms of the map (see Table 1 for details) and the color scale is in units of *Chandra* counts. The FWHM of the synthesized beam (effective resolution) is shown in the lower left corner. The E–W elongation is seen in both the SZA and *Chandra* data, and the peaks in the SZE and X-ray data align well.

(A color version of this figure is available in the online journal.)

(1) SZA data only, (2) *Chandra* data only, and (3) both the SZA and *Chandra* data jointly. Derived quantities such as mass and integrated SZE signal are computed within R_{500}, the radius within which the mean interior density is 500 times the critical density at the redshift of the cluster, $\rho_c(z) = 3H^2(z)/(8\pi G)$, where $H(z)$ is the Hubble parameter, and G is Newton's gravitational constant.

4.1.1. Chandra Spectroscopy for A2631

Both a single temperature and a temperature profile are measured for A2631. We extract spectra and response files for both data sets separately. Single-temperature spectra are extracted within $(0.15–1)R_{500}$ for the isothermal temperature analyses. The region used for spectroscopic extraction is found recursively, by picking a trial radius, extracting a spectrum to determine the electron temperature, T_e, within that radius, and computing $M_{500} \equiv M(R_{500})$ from hydrostatic equilibrium (Equation (3)) and the resulting R_{500}. This process is repeated until the values of the input and output R_{500} agree to 1%. Spectra are also extracted from within the full R_{500} determined as outlined above for comparison.

For the temperature profile, we extract spectra in radial annuli with $r_{\rm out}/r_{\rm in}$ set to a constant ratio. This follows Vikhlinin et al. (2006, hereafter V06) who found this choice produces roughly equal counts per annulus for cluster observations. However, we choose $r_{\rm out}/r_{\rm in} = 2$ (instead of 1.5 used by V06) in order to increase the counts in each radial bin, since our data have many fewer counts than the data considered in V06.

We construct quiescent ACIS background data sets by reprojecting the ACIS blank-field observations to match each data set. To account for variations in the particle background, the blank-field observations are scaled by the ratio of fluxes in the 9.5–12 keV band, where the *Chandra* effective area is essentially zero and the flux is due entirely to the background (e.g., Vikhlinin et al. 2005). Background spectra are extracted from these quiescent background data sets using the same regions as that for the cluster data and used when fitting the cluster spectral properties.

Table 3
A2631 *Chandra* Spectral Properties

$R_{\rm in}$ ($''$)	$R_{\rm out}$ ($''$)	T_e (keV)	Z ($Z_\odot$)
0	309	$7.9^{+0.5}_{-0.4}$	$0.38^{+0.14}_{-0.14}$
46	309	$7.3^{+0.6}_{-0.5}$	$0.42^{+0.13}_{-0.12}$
0	20	$8.3^{+2.2}_{-1.5}$	$1.12^{+0.54}_{-0.55}$
20	39	$8.1^{+1.3}_{-1.1}$	$0.38^{+0.31}_{-0.26}$
39	79	$9.9^{+1.2}_{-1.1}$	$0.49^{+0.22}_{-0.21}$
79	157	$7.8^{+0.8}_{-0.5}$	$0.48^{+0.22}_{-0.17}$
157	315	$6.7^{+0.6}_{-1.2}$	$1.22^{+0.36}_{-0.36}$
315	630	$6.0^{+1.5}_{-2.2}$	$0.88^{+1.64}_{-0.59}$

Notes. Fits performed with redshift $z = 0.27$ (Struble & Rood 1999) and Galactic H I column density $N_{\rm H} = 3.55 \times 10^{20}$ cm^{-2} (Kalberla et al. 2005).

Spectra for both *Chandra* observations using their respective responses are fit simultaneously to the same plasma model with the normalizations allowed to vary independently between data sets. Xspec (Arnaud 1996; Dorman & Arnaud 2001) is used to model the intracluster medium with an APEC spectrum (Smith et al. 2001) that includes bremsstrahlung and line emission components. We adopt the Galactic column density of $N_{\rm H} = 3.55 \times 10^{20}$ cm^{-2} (Kalberla et al. 2005), solar abundances of Asplund et al. (2009), and cross sections of Balucinska-Church & McCammon (1992) with an updated He cross section (Yan et al. 1998). The analysis uses data in the 0.7–7.0 keV energy range. The "cstat" statistic, which is similar to the Cash (1979) statistic, is used when modeling the spectral data to properly account for low counts.

Table 3 summarizes the *Chandra* spectral results, listing the inner and outer extraction radii, derived temperatures, T_e, and metallicity relative to solar, Z. In all cases, the model provides a good fit to the data, without any obvious structure or pattern in the residuals. As a check, the T_e profile spectra are fit fixing the metallicity to the global value ($Z = 0.4$). The resulting T_e's agree with those in Table 3 to within 1σ for all regions.

4.1.2. Cluster Models

For the SZA data, the clusters are fit with both the traditional β-model (Cavaliere & Fusco-Femiano 1976, 1978) and the universal pressure profile of Arnaud et al. (2010, hereafter A10). For the SZE-only β-model analysis, we fix $\beta = 0.86$ from a best fit to an average SZE profile (Plagge et al. 2010).

For the *Chandra* data, the cluster is fit with the traditional isothermal β-model and the modified β-model (e.g., V06) for density along with the corresponding V06 $T_e(r)$ profile, hereafter referred to as the V06 model. Many of the V06 model parameters must be fixed, given the large number of parameters compared with the quality of the X-ray data. A2631 does not show signs of a cool core so we excise those parts of the V06 model.

Joint fits to the SZA and *Chandra* data are performed by assuming the A10 pressure profile and a simplified, core-cut form of the V06 density profile (hereafter sV06) for the cluster models. These fits are performed both including and excluding the X-ray spectroscopic data, allowing the SZE and X-ray surface brightness data to place constraints on the cluster temperature (for details see Mroczkowski et al. 2009). The temperature is derived assuming the ideal gas law ($P_e = n_e k_B T_e$). The X-ray surface brightness data determine

the sV06 density fit, and the SZE surface brightness data drive the A10 pressure profile fit. A single temperature is derived from the inferred T_e profile using the prescription of Mazzotta et al. (2004) over the (0.15–1)R_{500} region. For the A10+sV06 fits that include spectroscopic information, the likelihood from the inferred T_e described above is included in the MCMC using the output from the *Chandra* single-temperature spectroscopy. A separate MCMC run is done without including the T_e spectral component in order to assess how X-ray surface brightness and SZE data can be used to find $M(r)$ without relying on X-ray spectroscopy.

4.1.3. Radio Point-source Model

The radio point-source model accounts for the primary beam attenuation and includes a spectral index that models the frequency dependence. The spectral dependence of the point source model is given by

$$F_\nu = F_{\nu_0}\left(\frac{\nu}{\nu_0}\right)^\alpha, \quad (1)$$

where F_ν is the intrinsic point-source flux density at frequency ν, F_{ν_0} is the intrinsic flux density at fiducial frequency ν_0, and α is the spectral index. We adopt the average frequency for the fiducial frequency, $\nu_0 = 30.938$ GHz, and report flux densities at this frequency.

Point sources are first modeled with both F_{ν_0} and α allowed to vary. The 8 GHz bandwidth of the SZA potentially provides leverage on both the spectral index and flux density of each point source. The flux density is, in general, well constrained. However, only weak constraints are obtained on α for all but the brightest sources. We first run fits including α in the Markov chain and then determine α using our 30 GHz flux density combined with 1.4 GHz flux densities from the NRAO VLA Sky Survey (NVSS; Condon et al. 1998). As a check, we compare the flux densities obtained using spectral indices from the combination of NVSS and SZA data just described to those obtained from the SZA data only. The flux densities are consistent within the 68% confidence regions.

4.1.4. Markov Chain Monte Carlo Analysis

We perform an MCMC analysis of the SZE and X-ray data (for details see Reese et al. 2000; Bonamente et al. 2004). The philosophy behind the analysis is to keep the data in a reduced but native state and to run the models through the observing strategy to compare directly to the data. Interferometers measure the Fourier transform of the sky brightness modulated by the primary beam. Therefore the SZA data most naturally provide constraints in the u–v plane, where the noise properties of the data and the spatial filtering of the interferometer are well understood. We perform model fits directly in the u–v plane, computing the Gaussian SZE likelihood, $\mathcal{L}_{\rm SZE}$. For X-ray data, the Poisson likelihood, $\mathcal{L}_{\rm X}$, is computed for each pixel, ignoring those that fall within the point source mask. The SZE and X-ray data are independent, and their likelihoods can simply be multiplied to obtain the combined likelihood. Best-fit parameters and confidence intervals are determined from the 50%, 16%, and 84% levels of the cumulative distribution function, which define the median and 68% confidence region. The resultant probability distributions are visually inspected, and convergence and mixing of the Markov chains are checked with the Geweke Z-statistic (Geweke 1992).

The cluster and any detected point sources in the field are modeled for the SZA data. The SZE signal varies as

$$\Delta T_{\rm SZE} = f(\nu) T_{\rm CMB} \int d\ell \frac{k_{\rm B} T_e}{m_e c^2} n_e \sigma_{\rm T} \equiv f(\nu) T_{\rm CMB}\, y, \quad (2)$$

where $f(\nu)$ is the frequency dependence of the SZE at frequency ν, n_e and T_e are the electron number density and temperature, $k_{\rm B}$ is the Boltzmann constant, m_e is the mass of the electron, $\sigma_{\rm T}$ is the Thomson cross section, integration is along the line of sight ℓ, and y is the Compton-y parameter. SZA data have sixteen 500 MHz bands covering 8 GHz of bandwidth. The frequency dependence of the SZE is taken into account when modeling. Relativistic corrections to $f(\nu)$ (e.g., Itoh et al. 1998; Challinor & Lasenby 1998) depend on T_e and are not included in this analysis for consistency, since only one cluster has a measured T_e. The effects of this small ($\lesssim$3% at 30 GHz) correction are discussed in Section 5.

For A2631, *Chandra* data are modeled with a cluster model and a constant X-ray background. Regions containing point sources are excluded from the fit.

4.1.5. Derived Cluster Properties

Derived quantities such as the integrated Compton-y, Y_{500}, and mass, M_{500}, are computed for each step in the Markov chain for each of the above types of fits we perform. We use these output chains to determine the median values and 68% confidence regions for each parameter of interest. This method cleanly propagates uncertainties from the parameters included in the chain. For example, uncertainties from modeling detected radio sources are propagated into the integrated Compton-y results.

We compute the integrated Compton-y, $Y_{\rm sph}(r) = \sigma_{\rm T}/(m_{\rm e}c^2)\int P_e dV$, within a spherical volume enclosed by radius r, where $dV = 4\pi r^2 dr$ and $P_e \equiv n_e k_{\rm B} T_e$ is the electron pressure. Since this latter quantity tracks thermal energy ($E = 3/2\int P_{\rm gas} dV$), and thermal pressure is the dominant source of support against gravitational collapse (see, e.g., Nagai et al. 2007; Lau et al. 2009, who report that only 10%–20% of the pressure comes from non-thermal support), we can expect $Y_{\rm sph}(r)$ to track gravitational energy within radius r. Assuming the virial relation, a constant gas fraction of 0.13, an average metallicity, and a total mass profile that can be described by a Navaro, Frenk, and White (NFW) halo model (Navarro et al. 1996, 1997), we estimate mass from fits to $Y_{\rm sph}(r)$ derived from our A10 and β-model fits to the SZE data (as was done in Mroczkowski 2011). These SZE-only mass estimates can be performed regardless of chosen model fit, and, like estimates from the X-ray assuming hydrostatic equilibrium, rely on spherical symmetry and do not take into account sources of non-thermal pressure support. We define $Y_{500} \equiv Y_{\rm sph}(R_{500})$ as the integrated Compton-y within R_{500}.

Mass estimates from the *Chandra* data are based on hydrostatic equilibrium (e.g., Sarazin 1988),

$$\begin{aligned} M(r) &= -\frac{k_{\rm B} T_e(r) r}{G\mu m_p}\left(\frac{d\ln(n_e)}{d\ln(r)} + \frac{d\ln(T_e)}{d\ln(r)}\right) \\ &= -\frac{r^2}{G\rho_{\rm gas}(r)}\frac{dP_{\rm gas}(r)}{dr}, \end{aligned} \quad (3)$$

where μ is the mean molecular weight, m_p is the mass of the proton, and $\rho_{\rm gas}$ and $P_{\rm gas}$ are the total gas density and pressure,

Table 4
Radio Point Sources

Field	R.A. (J2000) (h m s)	Decl. (J2000) (d m s)	R [a] (′)	F_{31} (mJy)	$F_{1.4}$ (mJy)	α	$F_{148}^{\rm est}$ (mJy)
ACTJ0022	00 22 13.006	−00 36 33.35	0.3	$1.33^{+0.15}_{-0.15}$	$18.8^{+0.7}_{-0.7}$	-0.9 ± 0.1	0.3
	00 22 05.987	−00 35 54.95	1.6	$0.98^{+0.13}_{-0.13}$	$33.2^{+1.1}_{-1.1}$	-1.1 ± 0.1	0.2
ACTJ2051	20 51 17.758	+00 53 20.16	2.3	$7.36^{+0.14}_{-0.14}$	$43.8^{+1.4}_{-1.4}$	-0.6 ± 0.1	3.0
	20 51 40.720	+00 52 02.74	7.3	$4.01^{+0.44}_{-0.44}$	$16.9^{+0.7}_{-0.7}$	-0.5 ± 0.1	1.9
A2631	23 37 40.209	+00 16 42.18	0.7	$3.99^{+0.16}_{-0.17}$	$107.0^{+3.8}_{-3.8}$	-1.1 ± 0.1	0.8
	23 37 38.106	+00 10 01.93	6.2	$3.20^{+0.34}_{-0.33}$	$12.4^{+0.6}_{-0.6}$	-0.4 ± 0.1	1.6

Note. [a] Projected distance from the cluster center.

Table 5
SZE and X-Ray Derived Properties

Field (model)	R_{500} (Mpc)	M_{500} ($10^{14}\ M_\odot$)	Y_{500} (10^{-4} Mpc^2)
ACTJ0022			
β–SZE	$0.92^{+0.02}_{-0.02}$	$5.7^{+0.4}_{-0.4}$	$0.85^{+0.12}_{-0.11}$
A10–SZE	$0.92^{+0.02}_{-0.02}$	$5.8^{+0.4}_{-0.4}$	$0.80^{+0.12}_{-0.10}$
A2631			
β–SZE	$1.27^{+0.11}_{-0.09}$	$8.3^{+2.3}_{-1.7}$	$1.22^{+0.68}_{-0.41}$
A10–SZE	$1.39^{+0.20}_{-0.16}$	$10.9^{+5.2}_{-4.8}$	$2.05^{+2.92}_{-1.04}$
β–X-ray	$1.31^{+0.03}_{-0.03}$	$8.5^{+0.8}_{-0.7}$	···
V06–X-ray	$1.54^{+0.10}_{-0.11}$	$13.8^{+2.9}_{-2.7}$	···
A10+sV06[a]	$1.33^{+0.20}_{-0.12}$	$9.4^{+4.8}_{-2.4}$	$1.03^{+0.31}_{-0.17}$
A10+sV06[b]	$1.31^{+0.35}_{-0.38}$	$9.1^{+9.4}_{-5.9}$	$1.01^{+0.65}_{-0.52}$

Notes.
[a] Includes X-ray spectroscopic information.
[b] Does not include X-ray spectroscopic information.

Table 6
ACT and SZA Central Compton-y Comparison

Cluster	Modeling	$y_0^{\rm ACT\,a}$ ($\times 10^{-4}$)	$y_0^{\rm SZA\,a}$ ($\times 10^{-4}$)	$y_0^{\rm ACT}/y_0^{\rm SZA}$
ACT-CL J0022–0036	SZA[b]	1.23 ± 0.14	1.22 ± 0.14	1.01
ACT-CL J2337+0016	SZA[b]	1.15 ± 0.14	1.17 ± 0.15	0.99
ACT-CL J2337+0016	joint[c]	1.15 ± 0.13	1.11 ± 0.11	1.03

Notes.
[a] ACT uncertainty is the map rms and SZA uncertainty is the parameter uncertainty from the MCMC analysis.
[b] SZA-only fits have fixed $\beta = 0.86$.
[c] Joint *Chandra* and SZA fit results.

respectively. The mass as a function of radius is used to compute R_{500} using $M_{500} \equiv M(R_{500}) = (4\pi/3)R_{500}^3 500\rho_c(z)$, where $\rho_c(z)$ is the critical density at redshift z. Our analysis is similar to that of Vikhlinin et al. (2006).

4.2. Results

The MCMC results for all detected point sources are presented in Table 4. In addition to the SZA 31 GHz flux densities, the corresponding NVSS (Condon et al. 1998) 1.4 GHz flux densities are listed. These two flux densities are used to compute the spectral index α, which is then used to estimate the point-source flux density in ACT's 148 GHz band, $F_{148}^{\rm est}$ (both also listed in Table 4). The projected distance from the cluster, R, is also listed and gives an idea of the potential impact of each source on cluster detection and potential contamination of the SZE flux. Table 5 summarizes the cluster modeling results for the SZA, *Chandra*, and joint analyses. We report R_{500}, M_{500}, and Y_{500} from our MCMC analysis.

Additionally, we compare the results of our fits to the SZA data with those obtained from matched filtering of the ACT maps. Table 6 compares the central Compton-y's, y_0, from the β-model matched filtered maps from ACT and the fit central decrements from the SZA data. The ACT data are calibrated to *WMAP* (Hajian et al. 2011) and SZA calibration is discussed in Section 3.2. Central Compton-y's are extracted from matched–filtered ACT maps by adopting the best-fit β-model from the SZA analysis as the filter. For the case of A2631, the β and core radius from the joint *Chandra* and SZA fit are also used as the β-model filter for the matched filter for comparison. The uncertainties on $y_0^{\rm ACT}$ are simply the rms's of the map while the uncertainties on $y_0^{\rm SZA}$ reflect the uncertainties on y_0 from the MCMC analysis. The ACT and SZA central decrements agree to within 3%, with 1% difference on average between the median values, well within 1σ. Since the other parameters from the β-model were held fixed, this indicates the integrated Compton-y values also agree at the same level.

Figure 3 shows the SZE u–v radial profiles of the SZA data (points) with best-fit β (blue) and A10 (red) models for ACTJ0022 (left) and A2631 (right). The visibilities (u–v plane data) are converted to a frequency-independent u–v plane Compton-y, Y_{uv}, and scaled by the angular diameter distance squared, $D_{\rm A}^2$, creating an SZE luminosity-like quantity (for details see, e.g., Mroczkowski et al. 2009). The real parts of Y_{uv} are plotted. The imaginary components are consistent with zero. Residuals are shown in the lower sections of both panels. The ACTJ0022 radial profile has $\chi^2 = 35.1$ and 35.8 with 28 degrees of freedom (dof) for the β and A10 models, respectively. The corresponding probabilities of obtaining these χ^2's or larger by chance given the degrees of freedom are, $p(\geqslant \chi^2|\,{\rm dof}) = 0.17$ and 0.15. The A2631 radial profiles have $\chi^2 = 38.1$ and 36.1 with 28 dof for the β and A10 models, respectively, with corresponding $p(\geqslant \chi^2|\,{\rm dof}) = 0.10$ and 0.14.

Figure 4 shows the *Chandra* surface brightness profile (upper) and temperature profile (lower) along with the best-fit models. The data (points) and best-fit β (blue) and V06 (red) models are shown. The best-fit background level is shown by the dotted line. The lower portion of each panel shows the residuals in units of the standard deviation. Despite this cluster's E–W elongation (Figure 2), a spherical model, on average, provides a good fit with $\chi^2 = 190.3$ and 155.9 for the β and V06 radial profiles that have 194 and 191 degrees of freedom (dof), giving $p(\geqslant \chi^2|\,{\rm dof}) = 0.56$ and 0.97, respectively. The V06

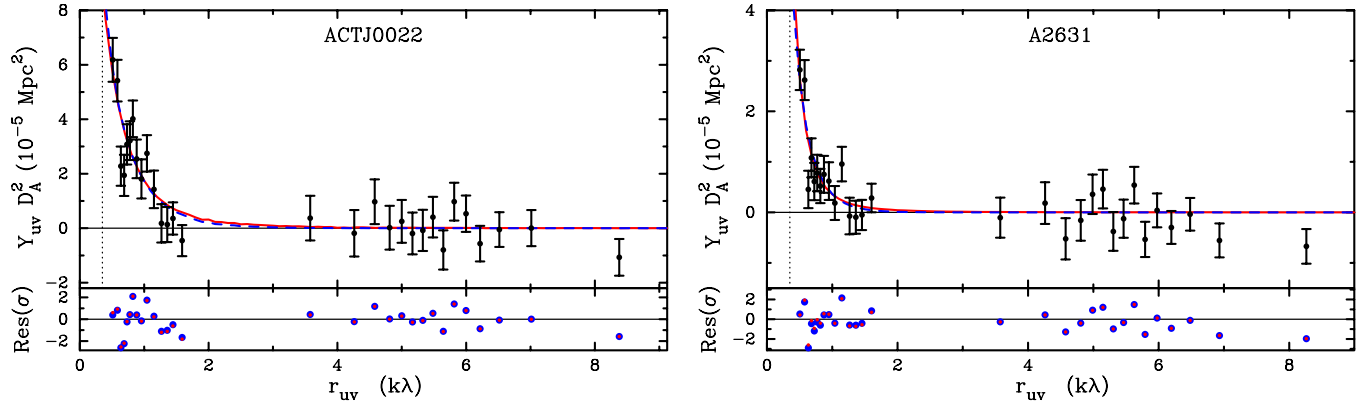

Figure 3. SZE profiles for ACTJ0022 (left) and A2631 (right) as a function of u–v radius, $r_{uv} = \sqrt{u^2 + v^2}$. Best-fit A10 (red) and β (blue) model fits are also shown. Residuals are shown in the lower sections in units of the standard deviation. Point sources have been subtracted from the visibilities and the phase centers shifted to the cluster centers before computing the profiles. The u–v plane Compton-y, Y_{uv}, is scaled by D_A^2, creating an SZE luminosity-like quantity (for details see, e.g., Mroczkowski et al. 2009). The real parts of Y_{uv} are shown. The imaginary parts are consistent with zero. The dotted line shows the shadowing limit of the 3.5 m dishes.

(A color version of this figure is available in the online journal.)

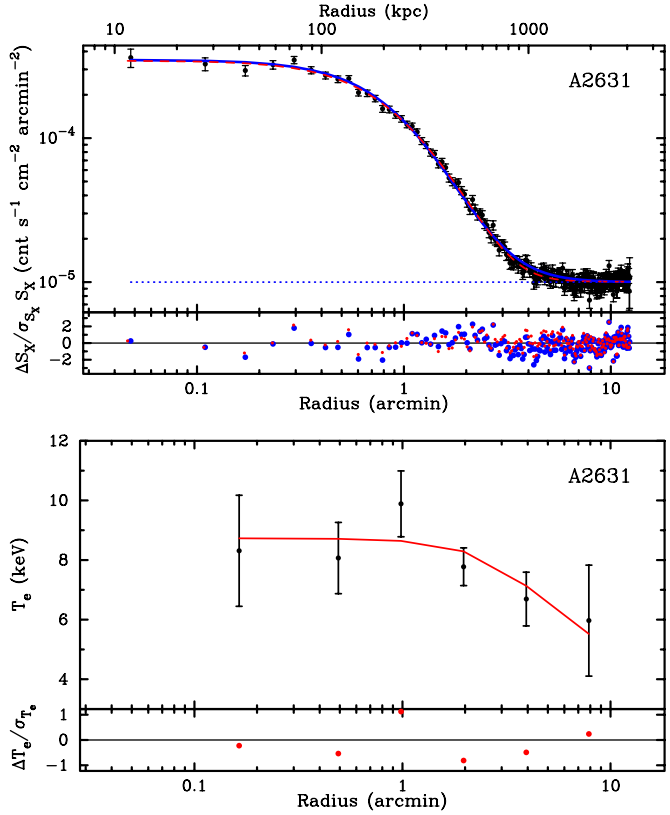

Figure 4. Upper: A2631 *Chandra* surface brightness profile (points) with best-fit β (blue) and V06 (red) models. The lower section shows residuals in units of the standard deviation. The models are similar and the simple spherical β-model provides a good fit to the *Chandra* data. The best-fit background level is shown by the dotted line. Lower: A2631 *Chandra* temperature profile (points) with best-fit V06 temperature (red) model. The lower section shows residuals in units of the standard deviation.

(A color version of this figure is available in the online journal.)

temperature profile results in $\chi^2 = 2.6$ for two degrees of freedom with $p(\geqslant \chi^2|\,\mathrm{dof}) = 0.27$.

Elliptical β-model fits to the SZA and *Chandra* A2631 data yield semi-minor to semi-major axial ratios of 0.51 ± 0.10 and 0.76 ± 0.01, respectively. Position angles (east of north) are $62^\circ \pm 7^\circ$ and $81^\circ \pm 2^\circ$ for the SZA and *Chandra* analyses, respectively. Both the X-ray and SZE fits yield changes in $-2\ln(L) \approx \chi^2$ that change significantly (>2) with the additional elliptical parameters, indicating the introduction of the additional parameters is justified when modeling the data. We use the radial profiles, where the counts in each bin are large, to assess goodness of fit via χ^2. The ellipticity is averaged over when constructing the radial profile, yielding similar goodness of fits results on the profiles for both circular and elliptical models.

The unknown orientation of the cluster with respect to the line of sight introduces a large uncertainty in the mass determination, since the full three-dimensional geometry of an ellipsoidal model is not constrained by the elliptical model fit. However, for a large, orientation-unbiased sample, the spherical assumption will, on average, provide accurate masses. The difference between the SZE and X-ray axial ratios is intriguing but inconclusive for only one cluster. We leave further study of departures from sphericity for a larger sample of clusters.

4.3. Optically Informed Cluster Properties

SDSS S82 data provide redshift information and enable mass estimates based on relations between cluster mass and optical properties such as richness and luminosity (e.g., Johnston et al. 2007; Reyes et al. 2008; Rozo et al. 2009). We have computed cluster masses from the $N_{200\overline{\rho}}$–M_{500} scaling relation of Rozo et al. (2009), which is based on weak-lensing and X-ray measurements of clusters from the SDSS maxBCG catalog (Koester et al. 2007). Masses computed from the $N_{200\overline{\rho}}$–M_{500} scaling relation of Reyes et al. (2008) yield similar results after correcting for the different radii used between the studies. M_{500} is the mass within R_{500}, as defined earlier, the radius within which the mean interior density is 500 times that of the critical density at the redshift of the cluster. $N_{200\overline{\rho}}$ is the number of red sequence galaxies in a cluster measured within $R_{200\overline{\rho}}$, the radius within which the mean interior density is 200 times the mean matter density at the redshift of the cluster, $\overline{\rho}(z) = \Omega_M(z)\,\rho_c(z)$, and is denoted by the subscript $\overline{\rho}$. $R_{200\overline{\rho}}$ at $z = 0$ corresponds to R_{60} (60 with respect to critical), and is substantially larger than R_{500} and R_{200}. Cluster $N_{200\overline{\rho}}$'s are computed for the S82 data using the maxBCG prescription as implemented by Menanteau et al. (2010b, see Section 2.2 for details). Table 7 summarizes the measured $N_{200\overline{\rho}}$ and inferred values of M_{500} and R_{500} for each cluster field.

Table 7
Optically Informed Properties

Field	$N_{200\bar{\rho}}$	M_{500} ($\times 10^{14}\ M_{\odot}$)	R_{500} (Mpc)	Y_{500} ($\times 10^{-4}$ Mpc^2)
ACTJ0022	113 ± 11	7.77 ± 1.12	1.03 ± 0.05	$0.84^{+0.11}_{-0.11}$
ACTJ2051	25 ± 5	1.54 ± 0.33	0.73 ± 0.05	...
A2631	77 ± 9	5.19 ± 0.75	1.11 ± 0.05	$1.43^{+1.01}_{-0.56}$

Notes. $N_{200\bar{\rho}}$'s are measured from SDSS S82 data, M_{500} is derived from $N_{200\bar{\rho}}$ using the scaling relation of Rozo et al. (2009), and R_{500} is inferred from the mass. This R_{500} is then used to compute Y_{500} from the SZA data for comparison to the Planck results (Planck Collaboration et al. 2011c).

A recent *Planck* study explores the SZE–optical scaling relations by employing a multi-frequency matched filter on *Planck* maps at the positions of the SDSS maxBCG clusters (Planck Collaboration et al. 2011c). That work finds an offset between the measured integrated Compton-y–optical-richness relation compared to model predictions for the full maxBCG sample. However, when using the X-ray subsample, the authors find good agreement between the prediction and the model. Following Planck Collaboration et al. (2011c), we determine R_{500} from the optical properties via the $N_{200\bar{\rho}}$–M_{500} relation (Table 7) and compute Y_{500} within that radius, using the fits of the A10 profile to the SZA data. Y_{500} is rescaled to redshift $z = 0$ using the evolution of the Hubble parameter for a flat universe, $E(z) = \sqrt{\Omega_M(1+z)^3 + \Omega_\Lambda}$, and a fiducial distance $D_A = 500$ Mpc, as

$$\tilde{Y}_{500} \equiv Y_{500} E(z)^{-2/3} (D_A(z)/500\,\mathrm{Mpc})^2\ [\mathrm{arcmin}^2]. \quad (4)$$

Figure 5 compares our two ACT clusters (red points) to those of *Planck* (black points) for the $\tilde{Y}_{500}$–$N_{200\bar{\rho}}$ relation. The best-fit power law for the *Planck* data over the full maxBCG catalog is also shown (line). The known X-ray cluster, A2631, lies above the *Planck* relation, though with large uncertainty.

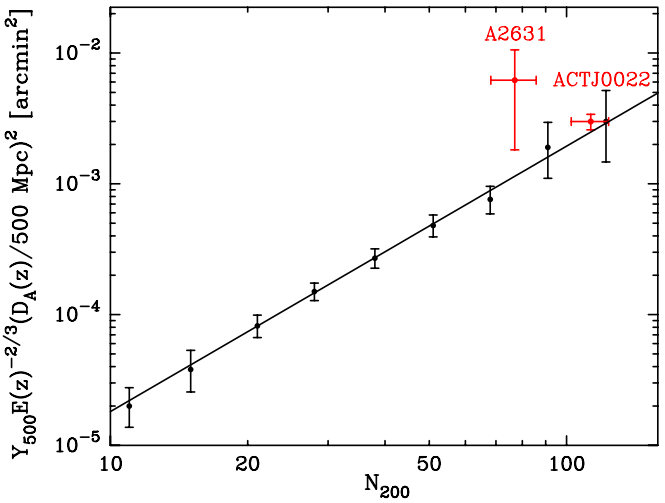

Figure 5. Integrated Compton-y–optical-richness relation, $\tilde{Y}_{500}$–$N_{200\bar{\rho}}$, for Planck (black) and this work (red). Also shown is the best-fit relation to the Planck data (solid line). Integrated Compton-y values are spherical values within R_{500} scaled to redshift zero and a distance $D_A = 500$ Mpc. Richness, $N_{200\bar{\rho}}$, is the number of red sequence galaxies within $R_{200\bar{\rho}}$.

(A color version of this figure is available in the online journal.)

5. DISCUSSION

The density of compact radio sources is higher in cluster regions compared to the field (Cooray et al. 1998; Massardi & De Zotti 2004; Lin & Mohr 2007; Coble et al. 2007). Contamination of the SZE signal from radio sources could potentially bias flux and mass estimates from the SZE. The radio source fluxes extrapolated to 148 GHz (Table 4) provide information on potential contamination of the SZE decrement signal. The two sources with projected radius from the cluster $R > 6'$ will have little impact on cluster detection and flux. ACT 148 GHz equatorial maps have a noise level of around 2 mJy beam^{-1} so that most sources are expected to fall well below the ACT map noise level, and the brightest source is expected to be 1.5 times the noise level. Very Large Array (VLA) observations of galaxies in nearby clusters between 5 and 40 GHz find that about 60% of the point sources show a flattening of the spectral shape above 8 GHz (Lin et al. 2009). This implies that extrapolating from low frequency to high frequency yields a lower limit on the contaminating flux. A conservative upper limit on the radio source flux density at 148 GHz is obtained by increasing the extrapolated estimates by a factor of two. However, recent simulations of the microwave sky suggest that only 3% of clusters have their 148 GHz SZE decrements contaminated at the $\gtrsim$20% level (Sehgal et al. 2010). There is no indication in the ACT data of contamination by sources in these three cluster fields. The estimated 148 GHz flux densities suggest that radio sources do not significantly impact cluster detection in surveys for the brightest clusters, although they could potentially bias flux measurements in some fraction of the clusters at a level of 3–6 mJy ($\lesssim$20% for typical -30 mJy integrated SZE fluxes). We reiterate that extrapolation to higher frequencies is uncertain and note that this is based on sources in only three cluster fields. More precise flux density estimates at ACT frequencies will be obtained through observing a larger number of ACT cluster fields over a range of frequencies.

The VLA FIRST survey (Becker et al. 1995) covers the ACTJ0022 and A2631 fields. Three out of the four radio point sources have NVSS and FIRST flux densities that agree within 68% confidence. The 107 mJy NVSS source in A2631's field has a 91 mJy flux density in the FIRST catalog, resulting in a predicted 148 GHz flux density that is 9% higher than that estimated from the NVSS flux density. These surveys are in different configurations and observe the same fields at different times, thus providing a rough handle on potential time variability of these sources, which could impact the contamination of the SZE signal and our use of point sources to calibrate our SZA data (Section 3.2). A 10% flux density variability is encompassed by our choice of a 20% calibration uncertainty for the SZA data.

The S82 data for ACTJ2051 exhibit a red sequence typical of galaxy clusters and provide a spectroscopic redshift. The optical mass estimates from the S82 data suggest that ACTJ2051 is less than a third of the mass of the other two clusters (Table 7). Using the *Planck* $\tilde{Y}_{500}$–$N_{200\bar{\rho}}$ relation, we estimate $Y_{500} = 2.7 \pm 1.2 \times 10^{-6}$ Mpc^2, which corresponds to $415 \pm 190\ \mu$Jy of integrated SZE flux within R_{500} at 31 GHz. This corresponds to an SZA signal smaller than 2σ for the observations considered here, below the SZA detection threshold. Furthermore, the above significance calculation assumes that the entire SZE flux within R_{500} is actually contained within the synthesized beam (effective resolution) of the SZA. However, the SZA synthesized beam is $1'.7$, smaller than R_{500} ($2'.6$) for this cluster, and the cluster SZE signal will be diluted.

Our mass estimates for ACTJ0022 and A2631 confirm that they are massive systems ($M_{500} \simeq 10^{15}\ M_{\odot}$). This is consistent

Table 8
Potential Systematics on Mass

Source	SZE (%)	X-ray (%)
Calibration	±10	±10
Asphericity	±10	±10
Clumping	−10	−10
Non-thermal P_e	+15	+15
Assumed f_g	±12	···
Relativisic corrections	+3	···
Total[a]	$^{+24}_{-21}$	$^{+21}_{-17}$

Note. [a] Added in quadrature.

with optical and X-ray follow-up of the initial cluster results from ACT's southern region that suggests the high-significance detections will be $\gtrsim 8 \times 10^{14}\ M_\odot$ (Menanteau et al. 2010a). The β and A10 model fits to the SZA data yield consistent masses for both clusters. The X-ray and joint mass estimates of A2631 also agree with the SZE estimates, to within $\lesssim 2\sigma$ in the worst case.

ACTJ0022 was discovered by ACT and we present initial mass estimates but there are previous X-ray analyses of A2631. Temperatures are computed from regions that differ between the different works. Using the earlier of the two *Chandra* observations, Maughan et al. (2008) find $T_e = 6.5 \pm 0.6$ keV within $(0.15–1)R_{500}$, where $R_{500} = 1.2$ Mpc. Analyses of *XMM-Newton* data using a number of methods for computing R_{500} yields $T_e = 7.5 \pm 0.5$ keV (within $(0.2–0.5)R_{500}$) and an average $M_{500} = (8 \pm 2) \times 10^{14}\ M_\odot$ within $R_{500} = 1.2$ Mpc (Zhang et al. 2008). Another analysis of *XMM-Newton* data finds $T_e = 7.7 \pm 0.6$ keV within an aperture containing 90% of the background-subtracted surface intensity (Andersson et al. 2009). Our derived $T_e = 7.3 \pm 0.6$ keV agrees to within 1.3σ with other *Chandra* and *XMM-Newton* measurements, despite the differences in radii. The Zhang et al. (2008) M_{500} is consistent with our derived SZE and X-ray masses to within 2σ in the most discrepant case. Despite data from various observatories and different methodologies, the temperatures and masses of A2631 are consistent.

A number of systematics may affect these mass measurements, summarized in Table 8 as percentages for a single cluster. Both simulation and analysis of X-ray data suggest that sphericity typically affects mass estimates at the 5%–10% level when measured at large radii such as R_{500} (e.g., Mathiesen et al. 1999; Piffaretti et al. 2003). We conservatively adopt 10% for the effects of asphericity. Simulations suggest that small-scale fluctuations, often called clumping, will cause a $\simeq$10% overestimate of mass (Mathiesen et al. 1999). Non-thermal pressure support may affect both SZE and X-ray mass estimates, causing mass to be underestimated at the 10%–20% level (e.g., Nagai et al. 2007; Lau et al. 2009). For the SZE-only analysis, changes in the assumed gas fraction, on average, change the mass by 12%, with lower gas fraction leading to higher mass; the fixed metallicity assumption is a $\leqslant$ 1% effect (Mroczkowski 2011), which we neglect. Relativistic corrections to the SZE are a 3% correction at 30 GHz for an 8 keV cluster like A2631 (Itoh et al. 1998).

The SZA and *Chandra* calibrations both affect the mass estimates. The SZE mass determinations depend on the SZE signal as $M \propto (\Delta T)^{1/2}$ so that the conservative 20% calibration results in a 10% change in mass. Recent changes in the *Chandra* calibration can change the cluster temperatures inferred from spectroscopic fits by $\simeq$10% (Reese et al. 2010; Nevalainen et al. 2010). This will directly impact our X-ray mass estimates since $M \propto T_e$.

Potential systematics are summarized in Table 8, with totals added in quadrature. Both SZE and X-ray estimates have potential systematics at the $\simeq$20% level, roughly the same order as the statistical uncertainties (Table 5).

6. CONCLUSION

We obtained SZA follow-up observations of three optically confirmed clusters from preliminary ACT maps along the celestial equator. ACT-CL J0022–0036 is a massive, high-redshift cluster newly discovered by ACT. The SZA detects two of the three clusters at high significance. ACT and SZA data show good qualitative agreement (Figure 1) and the central Compton-y values from the β-model analyses agree to well within 3%, with 1% difference on average between the median values (Table 6). The cluster A2631 shows good agreement between SZE and X-ray data (Figure 2) with both peaks aligning and similar E-W elongation seen in both wavebands. Initial mass estimates confirm that ACTJ0022 and A2631 are massive clusters with $M_{500} \simeq 10^{15}\ M_\odot$.

Two compact radio sources are detected by the SZA in each cluster field (Table 4). Using NVSS 1.4 GHz flux densities, we compute spectral indices and predict the flux densities in ACT's 148 GHz band. The radio sources are expected to be $\lesssim$6 mJy in the ACT 148 GHz maps, suggesting that radio sources are not a significant contaminant for detection of high mass clusters. However, they can still impact the measured SZE signal. As an example, the brightest source in A2631 could be filling in the SZE signal at the $\lesssim$20% level, assuming the extrapolation of the sources' lower-frequency flux densities holds. A more precise determination of potential contamination of the SZE signal from compact sources at ACT frequencies will be obtained through observing a larger number of ACT cluster fields over a range of frequencies.

Optimized for different purposes, ACT and SZA provide complementary SZE data on galaxy clusters. With the ability to quickly image large regions of the sky, ACT is well suited to finding clusters. Targeted observations with the SZA allow deep integrations for detailed cluster studies. The SZA images (Figure 1) show peak S/N of 12 and 10 for ACTJ0022 and A2631, respectively, compared to S/N $\simeq$ 6 for the match-filtered ACT images. The SZA provides higher resolution than ACT, measuring angular scales 15″–5′, well matched to clusters. In addition, the spatial filtering of the interferometer provides a clean method of disentangling cluster emission from radio point-source emission.

This pilot study of SZA follow-up observations of ACT-detected clusters shows that the detected clusters are massive systems. Cluster abundances are exponentially sensitive to mass (e.g., Press & Schechter 1974), with the most massive clusters providing the most leverage on cosmological studies. Finding extremely massive systems at high redshift can potentially rule out the current Λ-CDM paradigm (e.g., Mortonson et al. 2011). In addition, cosmological determinations utilizing massive systems are expected to be less susceptible to the effects of non-gravitational astrophysics. The highest mass systems from ACT's two survey regions will comprise our core sample for derivation of cosmological parameters from clusters. It is crucial to measure well the integrated SZE signal and the masses of these clusters for proper cosmological

interpretation of cluster yields from current and future SZE cluster surveys. Deep, targeted SZA observations provide a method of disentangling the point-source and cluster emissions and enable robust estimates of the integrated SZE signal, Y_{500}, and initial mass estimates. When combined with mass measures from X-ray and weak lensing, this will provide a robust measure of the mass–SZE flux scaling relation.

We are grateful to John Carpenter for guidance on CARMA observing, the queue, and a crash-course in Miriad. We thank the CARMA collaboration, especially Tom Plagge, for many discussions of the nitty-gritty details of the data. Support for T.M. was provided by NASA through the Einstein Fellowship Program, grant PF0-110077. The CARMA 3.5 m observations presented here were awarded in proposals c0563 and c0619.

This work was supported by the U.S. National Science Foundation through awards AST-0408698 for the ACT project, and PHY-0355328, AST-0707731, and PIRE-0507768. Funding was also provided by Princeton University and the University of Pennsylvania. The PIRE program made possible exchanges between Chile, South Africa, Spain, and the US that enabled this research program. Computations were performed on the GPC supercomputer at the SciNet HPC Consortium. SciNet is funded by the Canada Foundation for Innovation under the auspices of Compute Canada, the Government of Ontario, Ontario Research Fund–Research Excellence, and the University of Toronto. A.C.T. operates in the Parque Astronómico Atacama in northern Chile under the auspices of Programa de Astronomía de la Comisión Nacional de Investigación Científica y Tecnológica de Chile (CONICYT).

Support for CARMA construction was derived from the Gordon and Betty Moore Foundation, the Kenneth T. and Eileen L. Norris Foundation, the James S. McDonnell Foundation, the Associates of the California Institute of Technology, the University of Chicago, the states of California, Illinois, and Maryland, and the National Science Foundation. Ongoing CARMA development and operations are supported by the National Science Foundation under a cooperative agreement, and by the CARMA partner universities.

Funding for the SDSS and SDSS-II has been provided by the Alfred P. Sloan Foundation, the Participating Institutions, the National Science Foundation, the U.S. Department of Energy, the National Aeronautics and Space Administration, the Japanese Monbukagakusho, the Max Planck Society, and the Higher Education Funding Council for England. The SDSS is managed by the Astrophysical Research Consortium for the Participating Institutions. The Participating Institutions are the American Museum of Natural History, Astrophysical Institute Potsdam, University of Basel, University of Cambridge, Case Western Reserve University, University of Chicago, Drexel University, Fermilab, the Institute for Advanced Study, the Japan Participation Group, Johns Hopkins University, the Joint Institute for Nuclear Astrophysics, the Kavli Institute for Particle Astrophysics and Cosmology, the Korean Scientist Group, the Chinese Academy of Sciences (LAMOST), Los Alamos National Laboratory, the Max-Planck-Institute for Astronomy (MPIA), the Max-Planck-Institute for Astrophysics (MPA), New Mexico State University, Ohio State University, University of Pittsburgh, University of Portsmouth, Princeton University, the United States Naval Observatory, and the University of Washington.

This work made use of observations obtained with the Apache Point Observatory 3.5 m telescope, which is owned and operated by the Astrophysical Research Consortium and observations obtained at the Gemini Observatory, which is operated by the Association of Universities for Research in Astronomy, Inc., under a cooperative agreement with the NSF on behalf of the Gemini partnership.

This research has made use of the NASA/IPAC Extragalactic Database (NED) which is operated by the Jet Propulsion Laboratory, California Institute of Technology, under contract with the National Aeronautics and Space Administration. This research has made use of data obtained from the Chandra Data Archive and the CIAO software provided by the Chandra X-ray Center (CXC).

REFERENCES

Abazajian, K. N., Adelman-McCarthy, J. K., Agüeros, M. A., et al. 2009, ApJS, 182, 543
AMI Consortium, Hurley-Walker, N., et al. 2011, MNRAS, 414, L75
Andersson, K., Peterson, J. R., Madejski, G., & Goobar, A. 2009, ApJ, 696, 1029
Annis, J., Soares-Santos, M., Strauss, M. A., et al. 2012, arXiv:1111.6619
Arnaud, K. A. 1996, in ASP Conf. Ser. 101, Astronomical Data Analysis Software and Systems V, ed. G. H. Jacoby & J. Barnes (San Francisco, CA: ASP), 17
Arnaud, M., Pratt, G. W., Piffaretti, R., et al. 2010, A&A, 517, A92
Asplund, M., Grevesse, N., Sauval, A. J., & Scott, P. 2009, ARA&A, 47, 481
Bahcall, N. A., Fan, X., & Cen, R. 1997, ApJ, 485, L53
Balucinska-Church, M., & McCammon, D. 1992, ApJ, 400, 699
Bartlett, J. G., & Silk, J. 1994, ApJ, 423, 12
Becker, R. H., White, R. L., & Helfand, D. J. 1995, ApJ, 450, 559
Birkinshaw, M. 1999, Phys. Rep., 310, 97
Bonamente, M., Joy, M. K., Carlstrom, J. E., Reese, E. D., & LaRoque, S. J. 2004, ApJ, 614, 56
Borgani, S., Rosati, P., Tozzi, P., et al. 2001, ApJ, 561, 13
Carlstrom, J. E., Ade, P. A. R., Aird, K. A., et al. 2011, PASP, 123, 903
Carlstrom, J. E., Holder, G. P., & Reese, E. D. 2002, ARA&A, 40, 643
Cash, W. 1979, ApJ, 228, 939
Cavaliere, A., & Fusco-Femiano, R. 1976, A&A, 49, 137
Cavaliere, A., & Fusco-Femiano, R. 1978, A&A, 70, 677
Challinor, A., & Lasenby, A. 1998, ApJ, 499, 1
Coble, K., Bonamente, M., Carlstrom, J. E., et al. 2007, AJ, 134, 897
Condon, J. J., Cotton, W. D., Greisen, E. W., et al. 1998, AJ, 115, 1693
Cooray, A. R., Grego, L., Holzapfel, W. L., Joy, M., & Carlstrom, J. E. 1998, AJ, 115, 1388
Das, S., Marriage, T. A., Ade, P. A. R., et al. 2011, ApJ, 729, 62
Dorman, B., & Arnaud, K. A. 2001, in ASP Conf. Ser. 238, Astronomical Data Analysis Software and Systems X, ed. F. R. Harnden, Jr., F. A. Primini, & H. E. Payne (San Francisco, CA: ASP), 415
Dunkley, J., Hlozek, R., Sievers, J., et al. 2011, ApJ, 739, 52
Eke, V. R., Cole, S., Frenk, C. S., & Patrick Henry, J. 1998, MNRAS, 298, 1145
Fowler, J. W., Acquaviva, V., Ade, P. A. R., et al. 2010, ApJ, 722, 1148
Fowler, J. W., Niemack, M. D., Dicker, S. R., et al. 2007, Appl. Opt., 46, 3444
Geweke, J. 1992, in Bayesian Statistics IV, ed. J. M. B. et al. (Oxford: Clarendon), 169
Haehnelt, M. G., & Tegmark, M. 1996, MNRAS, 279, 545
Haiman, Z., Mohr, J. J., & Holder, G. P. 2001, ApJ, 553, 545
Hajian, A., Acquaviva, V., Ade, P. A. R., et al. 2011, ApJ, 740, 86
Henry, J. P. 2004, ApJ, 609, 603
Henry, J. P., & Arnaud, K. A. 1991, ApJ, 372, 410
Herranz, D., Sanz, J. L., Barreiro, R. B., et al. 2002, Proc. SPIE, 4847, 50
Holder, G. P., Mohr, J. J., Carlstrom, J. E., Evrard, A. E., & Leitch, E. M. 2000, ApJ, 544, 629
Itoh, N., Kohyama, Y., & Nozawa, S. 1998, ApJ, 502, 7
Johnston, D. E., Sheldon, E. S., Tasitsiomi, A., et al. 2007, ApJ, 656, 27
Kalberla, P. M. W., Burton, W. B., Hartmann, D., et al. 2005, A&A, 440, 775
Koester, B. P., McKay, T. A., Annis, J., et al. 2007, ApJ, 660, 239
Komatsu, E., Dunkley, J., Nolta, M. R., et al. 2009, ApJS, 180, 330
Komatsu, E., Smith, K. M., Dunkley, J., et al. 2011, ApJS, 192, 18
Lau, E. T., Kravtsov, A. V., & Nagai, D. 2009, ApJ, 705, 1129
Lin, Y., & Mohr, J. J. 2007, ApJS, 170, 71
Lin, Y., Partridge, B., Pober, J. C., et al. 2009, ApJ, 694, 992
Majumdar, S., & Mohr, J. J. 2004, ApJ, 613, 41
Mantz, A., Allen, S. W., Ebeling, H., & Rapetti, D. 2008, MNRAS, 387, 1179
Mantz, A., Allen, S. W., Rapetti, D., & Ebeling, H. 2010, MNRAS, 406, 1759

Marriage, T. A., Acquaviva, V., Ade, P. A. R., et al. 2011a, ApJ, 737, 61
Marriage, T. A., Baptiste Juin, J., Lin, Y.-T., et al. 2011b, ApJ, 731, 100
Massardi, M., & De Zotti, G. 2004, A&A, 424, 409
Mathiesen, B., Evrard, A. E., & Mohr, J. J. 1999, ApJ, 520, L21
Maughan, B. J., Jones, C., Forman, W., & Van Speybroeck, L. 2008, ApJS, 174, 117
Mazzotta, P., Rasia, E., Moscardini, L., & Tormen, G. 2004, MNRAS, 354, 10
Melin, J., Bartlett, J. G., & Delabrouille, J. 2006, A&A, 459, 341
Menanteau, F., González, J., Juin, J.-B., et al. 2010a, ApJ, 723, 1523
Menanteau, F., Hughes, J. P., Barrientos, L. F., et al. 2010b, ApJS, 191, 340
Mortonson, M. J., Hu, W., & Huterer, D. 2011, Phys. Rev. D, 83, 023015
Mroczkowski, T. 2011, ApJ, 728, L35
Mroczkowski, T., Bonamente, M., Carlstrom, J. E., et al. 2009, ApJ, 694, 1034
Muchovej, S., Leitch, E., Culverhouse, T., Carpenter, J., & Sievers, J. 2012, ApJ, 749, 46
Muchovej, S., Mroczkowski, T., Carlstrom, J. E., et al. 2007, ApJ, 663, 708
Nagai, D., Kravtsov, A. V., & Vikhlinin, A. 2007, ApJ, 668, 1
Navarro, J. F., Frenk, C. S., & White, S. D. M. 1996, ApJ, 462, 563
Navarro, J. F., Frenk, C. S., & White, S. D. M. 1997, ApJ, 490, 493
Nevalainen, J., David, L., & Guainazzi, M. 2010, A&A, 523, A22
Piffaretti, R., Jetzer, P., & Schindler, S. 2003, A&A, 398, 41
Plagge, T., Benson, B. A., Ade, P. A. R., et al. 2010, ApJ, 716, 1118
Planck Collaboration, Ade, P. A. R., et al. 2011a, A&A, 536, A1
Planck Collaboration, Ade, P. A. R., et al. 2011b, A&A, 536, A8
Planck Collaboration, Aghanim, N., et al. 2011c, A&A, 536, A12
Press, W. H., & Schechter, P. 1974, ApJ, 187, 425
Reese, E. D., Carlstrom, J. E., Joy, M., et al. 2002, ApJ, 581, 53
Reese, E. D., Kawahara, H., Kitayama, T., et al. 2010, ApJ, 721, 653
Reese, E. D., Mohr, J. J., Carlstrom, J. E., et al. 2000, ApJ, 533, 38
Reiprich, T. H., & Böhringer, H. 2002, ApJ, 567, 716
Rephaeli, Y. 1995, ApJ, 445, 33
Reyes, R., Mandelbaum, R., Hirata, C., Bahcall, N., & Seljak, U. 2008, MNRAS, 390, 1157
Rozo, E., Rykoff, E. S., Evrard, A., et al. 2009, ApJ, 699, 768
Rozo, E., Wechsler, R. H., Rykoff, E. S., et al. 2010, ApJ, 708, 645
Sarazin, C. L. 1988, X-ray Emission from Clusters of Galaxies (Cambridge Astrophysics Series; Cambridge: Cambridge Univ. Press)
Sault, R. J., Teuben, P. J., & Wright, M. C. H. 1995, in ASP Conf. Ser. 77, Astronomical Data Analysis Software and Systems IV, Vol. 4, ed. R. A. Shaw, H. E. Payne, & J. J. E. Hayes (San Francisco, CA: ASP), 433
Sayers, J., Czakon, N. G., Bridge, C., et al. 2012, ApJ, 749, L15
Schuecker, P., Böhringer, H., Collins, C. A., & Guzzo, L. 2003, A&A, 398, 867
Sehgal, N., Bode, P., Das, S., et al. 2010, ApJ, 709, 920
Sehgal, N., Trac, H., Acquaviva, V., et al. 2011, ApJ, 732, 44
Shepherd, M. C. 1997, in ASP Conf. Ser. 125, Astronomical Data Analysis Software and Systems VI, ed. G. Hunt & H. Payne (San Francisco, CA: ASP), 77
Smith, R. K., Brickhouse, N. S., Liedahl, D. A., & Raymond, J. C. 2001, ApJ, 556, L91
Story, K., Aird, K. A., Andersson, K., et al. 2011, ApJ, 735, L36
Struble, M. F., & Rood, H. J. 1999, ApJS, 125, 35
Sunyaev, R. A., & Zeldovich, I. B. 1980, ARA&A, 18, 537
Sunyaev, R. A., & Zel'dovich, Y. B. 1970, Comments Astrophys. Space Phys., 2, 66
Sunyaev, R. A., & Zel'dovich, Y. B. 1972, Comments Astrophys. Space Phys., 4, 173
Swetz, D. S., Ade, P. A. R., Amiri, M., et al. 2011, ApJS, 194, 41
Vanderlinde, K., Crawford, T. M., de Haan, T., et al. 2010, ApJ, 722, 1180
Viana, P. T. P., & Liddle, A. R. 1996, MNRAS, 281, 323
Vikhlinin, A., Kravtsov, A. V., Burenin, R. A., et al. 2009, ApJ, 692, 1060
Vikhlinin, A., Kravtsov, A. V., Forman, W., et al. 2006, ApJ, 640, 691
Vikhlinin, A., Markevitch, M., Murray, S. S., et al. 2005, ApJ, 628, 655
Williamson, R., Benson, B. A., High, F. W., et al. 2011, ApJ, 738, 139
Yan, M., Sadeghpour, H. R., & Dalgarno, A. 1998, ApJ, 496, 1044
Zeldovich, Y. B., & Sunyaev, R. A. 1969, Ap&SS, 4, 301
Zhang, Y.-Y., Finoguenov, A., Böhringer, H., et al. 2008, A&A, 482, 451